# Activity and stability studies of platinized multi-walled carbon nanotubes as fuel cell electrocatalysts

Serban N. Stamatin [a,*], Maryam Borghei [b], Rajnish Dhiman [a], Shuang Ma Andersen [a,*], Virginia Ruiz [c], Esko Kauppinen [b], Eivind M. Skou [a]

[a] Institute of Chemical Engineering, Biotechnology and Environmental Technology, University of Southern Denmark, Niels Bohrs Alle 1, Odense, DK-5230, Denmark
[b] NanoMaterials Group, Department of Applied Physics, Aalto University, Puumiehenkuja 2, 02150 Espoo, Finland
[c] CIDETEC-IK4, Centre for Electrochemical Technologies, Paseo Miramon 196, E-20009 Donostia-San Sebastian, Spain

## ARTICLE INFO

## ABSTRACT

A non-covalent functionalization for multi-walled carbon nanotubes has been used as an alternative to the damaging acid treatment. Platinum nanoparticles with similar particle size distribution have been deposited on the surface modified multi-walled carbon nanotubes. The interaction between platinum nanoparticles and multi-walled carbon nanotubes functionalized with 1-pyrenecarboxylic acid is studied and its electrochemical stability investigated. This study reveals the existence of a platinum-support interaction and leads to three main conclusions. First, the addition of 1-pyrenecarboxylic acid is improving the dispersion of platinum nanoparticles, leading to an improved electrochemical activity towards oxygen reduction reaction. Second, the investigations regarding the electrochemical stability showed that the platinum-support interaction plays an important role in improving the long-term stability by as much as 20%. Third, post-mortem microscopy analysis showed a surprising effect. During the electrochemical stability investigations concerned with carbon corrosion it was found that the multi-walled carbon nanotubes were undergoing severe structural change, transforming finally into carbon spheres.

© 2014 Elsevier B.V. All rights reserved.

## 1. Introduction

Efficient electrochemical conversion of energy has an utmost importance in answering the needs of future energy supply and demands. In this respect, polymer electrolyte fuel cells (PEMFCs) represent a research avenue, due to the fact that it can produce electrical and thermal energy in a versatile way. Usually, low temperature PEMFCs are using electrocatalysts in the form of nanoparticles supported on high surface area carbons. Pt based materials are the most used electrocatalysts in a real PEMFC. Even with the steady decrease in the Pt price over the last 2 years [1], Pt price is still one of the main drawbacks for PEMFC commercialization. Having these said, huge efforts have been made for developing PEMFC with non-precious metal catalysts [2,3]. However, from the performance point of view the Pt based materials supported on high surface area carbons have a superior activity compared to the non-precious metal catalysts. In order to achieve the US Department of Energy mass activity targets [4], Pt alloying with several transition metals has been explored [5–8]. Nevertheless, the deployment of PEMFCs is still limited by several key aspects related to overall cost and performance loss during extended operation time. It was proven recently that Pt dissolution is a major degradation mechanism along with Ostwald ripening, support corrosion, particle migration and coalescence [9]. Nonetheless, one should consider the degradation mechanisms associated with the electrocatalyst/support system.

Even though the direct degradation of Pt is the most studied phenomenon, carbon corrosion can play an important role in the overall degradation of the catalyst especially when potential spikes up to 1.44 $V_{RHE}$ are occurring during start-up/shutdown [10]. During these periods the high surface area carbon undergoes severe electrochemical corrosion. According to its Pourbaix diagram, carbon is not stable under PEMFC operating conditions when exposed to potentials larger than 0.207 $V_{RHE}$ [11]. Yet, no corrosion is taking place at these low potentials due to the sluggish kinetics, but carbon corrosion is accelerated by the presence of Pt at larger potentials and elevated temperature. In this respect, much effort has been made for replacing the carbon support with different ceramics [12–18]. From the research point of view, the ideal

support should have a property matrix consisting of high surface area, high electronic conductivity and high resistance towards corrosion under PEMFC operating conditions. Even if an alternative material to carbon is found having the above mentioned property matrix, it will probably still take some time before it may be replaced in a real PEMFC manufacturing industry due to the membrane-electrode assembly (MEA) optimization and probably higher costs of the support, itself. This is why carbon materials with alternative structures [19–22] are still the most viable solution. Multiwalled carbon nanotubes (MWCNTs) were among the first alternative carbon nanostructures to be tested as PEMFC electrocatalyst support [23,24] due to their large surface area and remarkable electronic conductivity.

Electrochemical corrosion of carbon is known to take place during PEMFC operating conditions, even though the full corrosion process is not completely understood. It is widely acknowledged that amorphous carbon defects are formed at large potentials and corroded at lower potentials [25]. Carbon oxidation starts with the presence of defects or at the kinks of the basal planes which have unsaturated valences and free σ-electrons [26]. The defects are crystallographic sites with different reactivity. Considering that MWCNTs have a relative defect-free structure it should be a rather stable material which does not undergo severe corrosion under PEMFC operating conditions. However, this defect-free structure translates into no anchoring points for Pt, thus functionalization is needed prior to Pt deposition. Covalent functionalization has been widely used in this respect [27], where the use of highly concentrated sulphuric acid, nitric acid, or a mixture between these two, oxidizes the MWCNT surface creating different oxygen functional groups. Nonetheless, this harsh treatment causes permanent damage to the MWCNT structure resulting in a large amount of surface defects which may be one of the starting points for the overall carbon oxidation.

There are several studies available in literature which considers MWCNT as possible electrocatalyst support for PEMFC. For example, heat treated MWCNTs perform better than the untreated MWCNTs in terms of activity and durability [28]. Another study shows that the diameter of the MWCNTs plays an important role, MWCNTs with a larger diameter have an increased specific activity and improved durability [29]. Zhao et al. showed that MWCNT with a specific surface area of $120 \, m^2 \, g^{-1}$ are the most suitable MWCNTs as PEMFC electrocatalyst support [30]. It is difficult to compare results among different research groups for several reasons. First, most of the studies are performing cyclic voltamograms in either sulphuric acid or perchloric acid which results in different oxygen reduction reaction (ORR) activity. Since anion adsorption may influence the catalyst activity [31], it is preferred to electrochemically test the materials in perchloric acid and not in sulphuric acid. Second, the lack of similar Pt nanoparticle size supported on different supports can result in different degradation mechanisms which may lead to an erroneous conclusion. It is a well-known fact that smaller nanoparticles increase the surface energy leading to a faster Pt degradation rate [32]. Modifying both the particle size and the support will result in ambiguous conclusions. Supports which have a large difference in surface area in comparison to the reference support may automatically result in a preferential degradation mechanism. Third, the use of different accelerated stress test (AST) might have a different outcome for identical materials, which makes it difficult to compare results among different research groups. Therefore this paper aim is to prove that it is possible to increase the durability and ORR activity of Pt supported on MWCNTs just by enhancing the nanoparticle dispersion on the support without modifying the particle size or subjecting the MWCNTs to harsh acid treatments.

In this work, a non-covalent functionalization with 1-pyrenecarboxylic acid (PCA) has been used in order to maintain the pristine MWCNT surface characteristics. Pt in the form of nanoparticles has been synthesized beforehand and subsequently deposited on the non-covalently functionalized MWCNT surface. The present study focuses on the interaction between the Pt nanoparticles, MWCNTs and the PCA which is attached on the carbon nanotubes. In this respect, a wide range of physico-chemical characterization techniques were used to explain the findings resulted from the electrochemical activity and stability measurements. In our attempt to provide proof that the interaction between Pt, MWCNT and PCA is enhancing the electrochemical stability, we have observed an unexpected effect, mainly segmenting the graphene layers constituting the MWCNT.

## 2. Experimental

### 2.1. Materials

MWCNTs (BET: $270 \, m^2 \, g^{-1}$; VGCF-X$^{TM}$, Showa Denko, Japan) were used as starting support material and have been used without further purification. Ethylene glycol (EG, 99%, VWR), $K_2PtCl_4$ (46.75%, Alfa-Aesar) polyvinylpyrrolidone with $M_w = 55,000$ (PVP, Sigma Aldrich), 1-pyrenecarboxylic acid (PCA, 97%, Sigma-Aldrich), acetone (99%, VWR) and ethanol (96%, VWR) were used for platinization of MWCNT without any further purification. Perchloric acid (TraceSelect®, Sigma Aldrich) and ultrapure water (18.2 MΩ, Millipore) were used for the preparation of the electrolyte.

### 2.2. Synthesis

150 mg of MWCNTs were added to 10 ml of ethanol along with 0, 1.5, 3 and 7.5 mg of PCA and ultrasonicated (Bandelin SONOREX$^{TM}$) for 1 h in order to produce MWCNT with 0%, 1%, 2% and 5% PCA, respectively. The solvent was evaporated prior platinization. PCA was previously used to obtain a better dispersion of MWCNT in different solutions [33]. Pt nanoparticles were synthesized via a modified polyol method previously reported elsewhere [17]. Briefly, a volume of 20 ml of 9.6 mM $K_2PtCl_4$ in EG was vigorously stirred at room temperature with 20 ml solution of 6 mM PVP in EG until complete dissolution of PVP and $K_2PtCl_4$ in EG was achieved. The resulting mixture was refluxed at 160 °C with Ar purging. After 3 h, the mixture was cooled to room temperature, and 150 mg of the desired support material was added along with 300 ml of acetone and magnetic stirred for 12 h. The final solution was centrifuged 6 times at 4500 rcf (Eppendorf 5804) and vacuum dried for 12 h at 90 °C. The final samples were denoted as Pt/MWCNT-PCA-0%, Pt/MWCNT-PCA-1%, Pt/MWCNT-PCA-2% and Pt/MWCNT-PCA-5%, respectively.

### 2.3. Physical characterization

Thermo gravimetric analyses (TGA) were performed using a Netzsch STA-449-F3 equipped with a Pt sample carrier placed vertically in a furnace. The samples were placed in an alumina crucible and heated to 1000 °C with a 20 K min$^{-1}$ heating rate in a gas mixture consisting of nitrogen supplied at 40 ml min$^{-1}$ and oxygen supplied at 10 ml min$^{-1}$.

X-ray diffraction (XRD) analysis was carried out by means of X'Pert Pro PANalytical X-ray diffractometer. The analysis took place between 10° and 85° glancing angles with a 0.02° step and a dwelling time of 12 s per step. The peaks were compared against the powder diffraction files (PDF) standardized by the International Centre for Diffraction Data (ICDD) for phase identification purposes.

The surface studies were carried out by using X-ray photoelectron spectrometer (XPS) from SPECS® by using the Mg $K\alpha$ source and the data was analysed by using CasaXPS$^{TM}$ software. The survey spectra (resolution of 2.5 eV) were recorded for kinetic energies
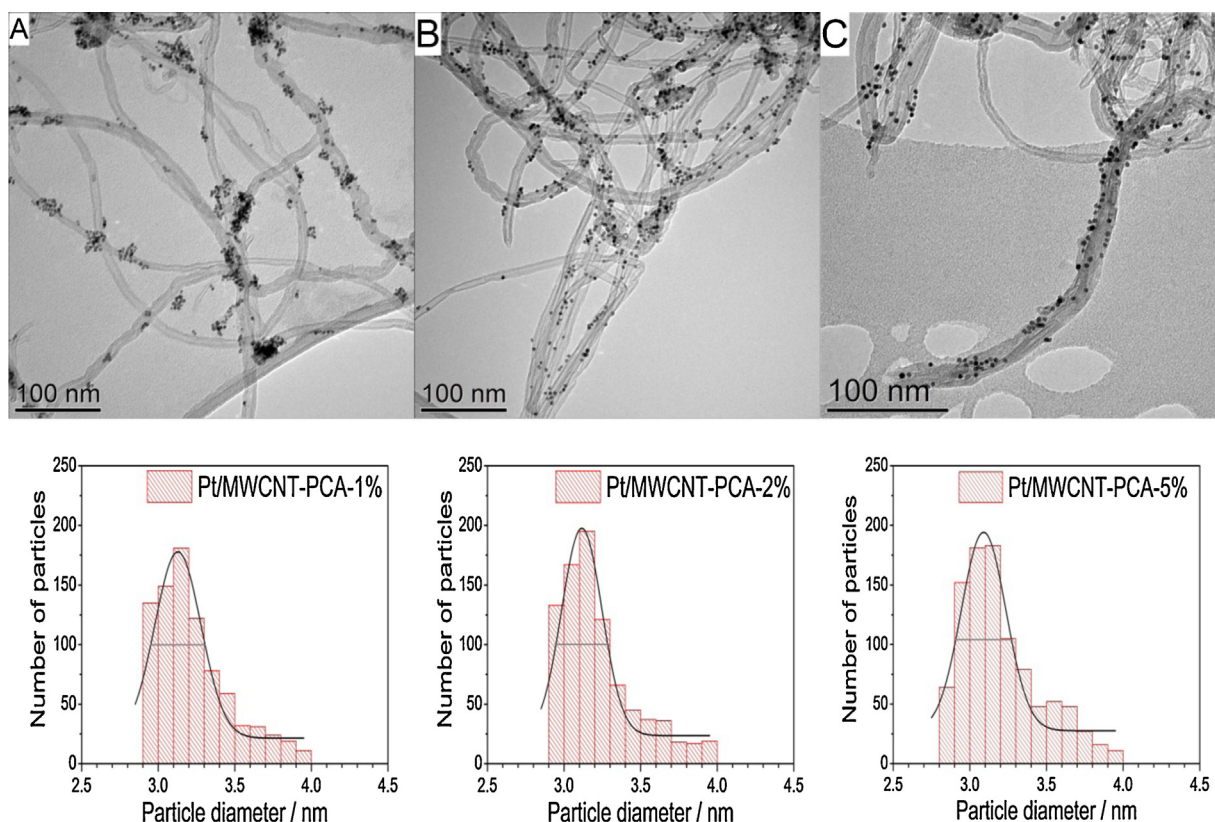
**Fig. 1.** TEM images of Pt/MWCNT-PCA-1% (A), Pt/MWCNT-PCA-2% (B) and Pt/MWCNT-PCA-5% (C) with the corresponding histograms below each picture. The histograms were obtained from several pictures of the same sample until approx. 1000 particles were analysed. The FWHM are indicated in the corresponding histograms by a grey line.

from 200 eV to 1260 eV. The deconvolution of high resolution spectra (resolution of 1.3 eV) has been done by fitting the peaks to pure Gaussian peaks using Shirley background.

Transmission electron microscopy (TEM) was performed at 120 kV by means of Tecnai 12 Bio Twin equipped with a $LaB_6$ gun.

### 2.4. Electrochemical characterization

All the electrochemistry characterization was performed in an all glass two-compartment three electrode setup, where a rotating disk electrode (RDE, Pine Instruments) with a 0.196 $cm^2$ glassy carbon electrode insert was the working electrode. The reference electrode was a dynamic hydrogen electrode (Hydroflex®, Gaskatel) while the counter electrode was made out of a Pt coil encapsulated in a glass tube with a ceramic frit. All the potentials are listed against the reversible hydrogen electrode (RHE). For each experiment, 200 ml of freshly prepared 0.1 M $HClO_4$ was prepared with ultrapure water and used as an electrolyte. A Zahner® IM6-Ex potentiostat controlled by Thales (Zahner®) was used for the ORR measurements, while a Pine Instruments potentiostat was used for the extended durability measurements.

All the inks were prepared with ultrapure water (>18.2 M$\Omega$, Millipore) and had a Pt concentration of 0.10 $mg_{Pt}$ $cm^{-3}$. The catalyst was dispersed in ultrapure water by 1 h ultrasonication and prior to the electrochemical measurements it was ultrasonicated 30 min. The working electrode was polished to a mirror finish and 10 $\mu$l of ink was drop coated on its surface resulting in a loading of 10 $\mu g_{Pt}$ $cm^{-2}$, 20 $\mu g_{Pt}$ $cm^{-2}$ were used for the AST. iR compensation was performed by positive feedback until the electrolyte resistance was less than 2 $\Omega$. The samples were cycled for 200 cycles at 0.2 V $s^{-1}$ between 0.05 and 1.3 $V_{RHE}$ prior to testing. Cyclic voltammograms (CVs) were recorded at 0.05 V $s^{-1}$ between 0.05

and 1.3 $V_{RHE}$ in an argon saturated electrolyte with a 0.002 V resolution. In order to determine the electrochemical surface area (ESA), the charge associated with the anodic region between 0.05 and 0.4 $V_{RHE}$ was calculated with subtraction of the charge associated with the double layer and, finally, divided by 210 $\mu C$ $cm^{-2}$. The specific electrochemical surface area (ECSA) was obtained by dividing the ESA with the Pt electrode mass. AST I was performed in Ar saturated electrolyte between 0.05 and 1.3 $V_{RHE}$ with a sweeping rate of 0.2 V $s^{-1}$ for 5000 cycles. AST II was performed in Ar saturated electrolyte between 1 and 1.5 $V_{RHE}$ with a sweeping rate of 0.5 V $s^{-1}$ for 30,000 cycles (approx. 17 h). This is part of the FCCJ (Fuel Cell Commercialization Conference of Japan) two-step protocol [34] which is widely acknowledged in the literature to separate the electrocatalyst degradation from the support degradation. The ESA was measured every 500 cycles by cycling the working electrode between 0.05 and 1.3 $V_{RHE}$ at 0.2 V $s^{-1}$ for 10 cycles.

## 3. Results and discussion

### 3.1. Physico-chemical characterization

Fig. 1 shows TEM images of Pt supported on MWCNT with 1%, 2% and 5% PCA along with the TEM particle histograms. Fig. S1 (Supplementary data, Appendix A) shows the TEM images of Pt/MWCNT-PCA-0% where large agglomerates of Pt nanoparticles are seen (blue coloured ellipses in Fig. S1), leaving a large part of the MWCNT surface uncovered by Pt which will lead to a rather poor activity and durability. Therefore, further physico-chemical characterization has been abandoned from this work. As it can be seen from the TEM particle histograms the Pt nanoparticles follow a Gaussian distribution where the peak centre is 3.1 nm and a spread
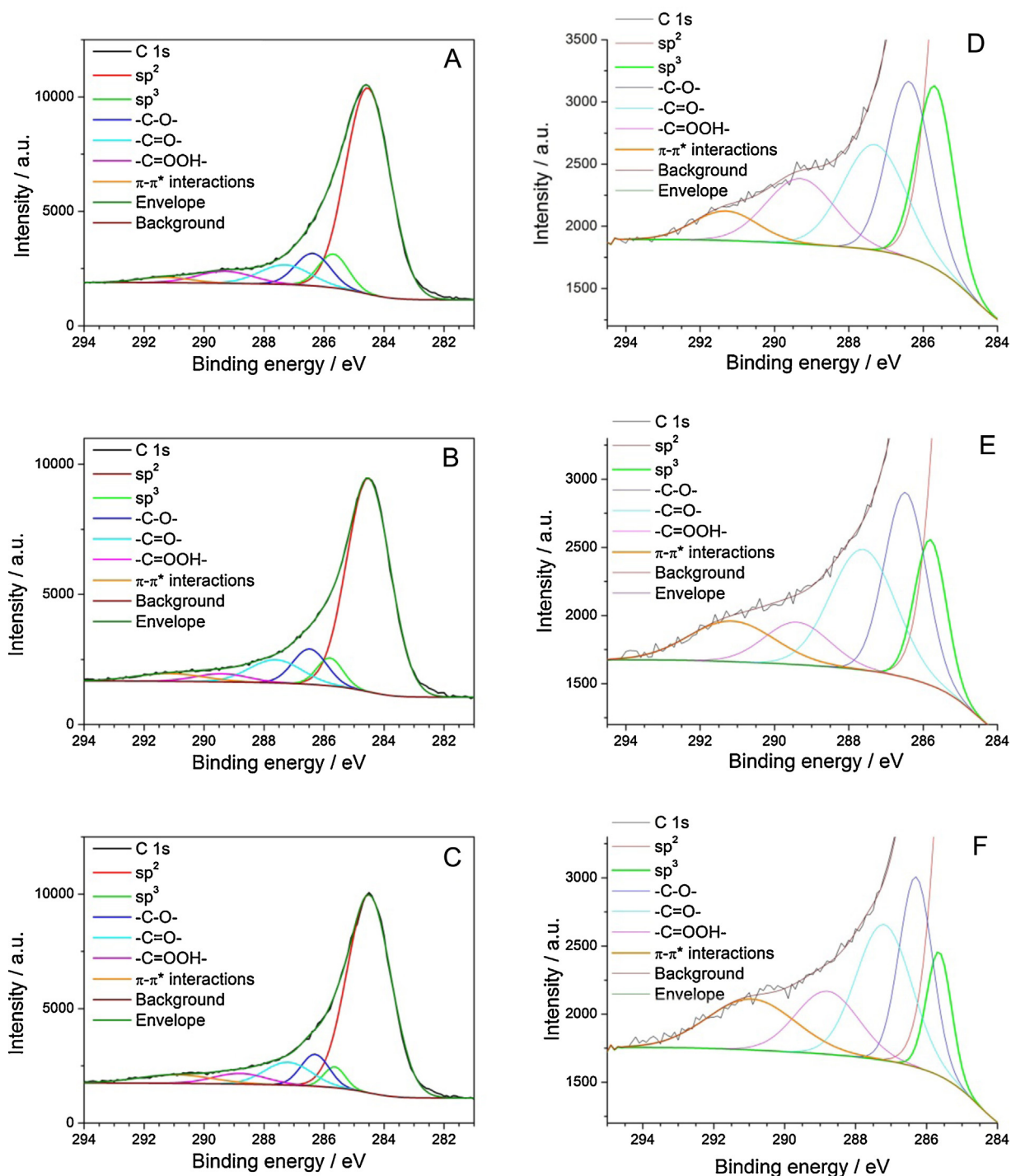
**Fig. 2.** Deconvolution of the C 1s peak obtained from the XPS analysis of Pt/MWCNT-PCA-1% (A), Pt/MWCNT-PCA-2% (B) and Pt/MWCNT-PCA-5% (C). Enlarged C 1s peak Pt/MWCNT-PCA-1% (D), Pt/MWCNT-PCA-2% (E) and Pt/MWCNT-PCA-5% (F).

of approx. 0.4 nm (the FWHM of the Gaussian fit was considered the spread). This is very close to the crystallite size obtained from the Pt (1 0 0) peak present in the XRD spectrum (Fig. S2, Supplementary data, Appendix A). Using the Scherrer formula for Pt (1 0 0), located at approx. $2\theta = 40°$, which indicates a crystallite size of approx. 2.9 nm for all the samples. Considering that similar Pt nanoparticles were obtained for surface modified support, it can be concluded that the Pt nanoparticle synthesis is highly reproducible. It is highly important for the tested materials to have similar Pt nanoparticle size distribution in order for the electrochemical performance not to be flawed. In contrast to Pt/MWCNT-PCA-0%, the Pt dispersion

on the MWCNT surface is improving with the increase of PCA. By adding just the equivalent of 1% PCA to the MWCNT surface the dispersion improves, nevertheless Pt/MWCNT-PCA-1% still has small Pt islands formed of Pt nanoparticles, while for Pt/MWCNT-PCA-2% and Pt/MWCNT-PCA-5% the particle dispersion is improved leading to almost no particle agglomeration. It is expected that the activity and durability of these samples will improve with increasing PCA content.

An extended XPS description with regards to peak positions and deconvolution method is presented in Supporting Information. The C 1s XPS survey, presented in Fig. 2, shows that the PCA modifies

the surface composition of MWCNT. The deconvolution of the C 1s peak (Table 1) supports the proposed mechanism of $\pi$–$\pi^*$ interaction between the MWCNT and the PCA. It is clear that increasing the PCA amount leads to an increase in the $\pi$–$\pi^*$ interaction. There is significant increase in the contribution of $\pi$–$\pi^*$ interaction from 2.1 to 5.2% in C 1s deconvolution. The concentration of C—C bonding (corresponding to the sp$^2$ hybridization) slightly increases from 69.2% for Pt/MWCNT-PCA-1% until 70.8% for Pt/MWCNT-PCA-5% (Table 1). There is slight decrease in the binding energy of C—C towards low binding energy which indicates the graphitization with increased amount of PCA. This was expected, mainly due to the presence of more carbon rings on the surface resulted from the increase of PCA. The relative concentration of surface defects (corresponding to sp$^3$ hybridizarion because of the presence of dangling bonds) considerably decreases with increasing the amount of PCA, which could be due to the coverage of the MWCNTs surface with the pyrene molecules. PCA molecules are highly graphitized due to the presence of four benzene rings. The surface concentrations of C=O, C=O and C=OOH bonds are more or less similar in amount for all the samples due to the similar environment of functionalised groups. One should bear in mind that there is 1 carboxylic group per each 16 carbon atoms in PCA, which is why there is little difference in the surface concentrations of C=O, C=O and C=OOH. The amount of Pt from survey spectra are 0.67, 0.82 and 1.0% for Pt/MWCNT-PCA-1%, Pt/MWCNT-PCA-2% and Pt/MWCNT-PCA-5%, respectively. This increasing trend can easily be explained on the basis of Fig. 1, which shows the better dispersion of Pt on MWCNTs with increasing amount of PCA and thus makes it easily available for electrochemical processes. The Pt 4f peak (Fig. S3) shows that the overall surface concentration of metallic Pt (Pt$^0$) is decreasing with increasing PCA amount (Table 1), which might be caused by Pt coverage with excess PCA. These findings have not been proposed in previous works involving PCA interactions with either MWCNTs [22] or CNFs [36]. These are clear indications that Pt interacts with the carboxylic moieties present in the PCA, which can be the foundation of the improved durability for these types of material. Moreover this is supported by both the overall concentration of Pt$^{(2+)}$ and Pt$^{(4+)}$ from the Pt 4f peak as well as from the surface concentration of PtO$_2$ from the O 1s peak (Fig. S3).

### 3.2. Electrochemical performance

The Pt electrode loading was obtained from the Pt loading on the MWCNTs as obtained from TG analysis (Fig. S4, Supplementary data, Appendix A), which was approx. 20% for all the samples. The increase in the specific electrochemical surface area (ECSA) can be clearly seen from Fig. S5 (Supplementary data, Appendix A) which shows the cyclic voltammograms (CVs) obtained for Pt/MWCNT-PCA-1%, Pt/MWCNT-PCA-2% and Pt/MWCNT-PCA-5%. To accurately reflect only the role played by the PCA on the MWCNT surface, the voltammograms were normalized to the geometrical area of the electrode (0.196 cm$^{-2}$) and the Pt electrode loading. 20 $\mu$g$_{Pt}$ cm$^{-2}$ was needed for achieving a good electrode in the case of Pt/MWCNT-PCA-1%. The CV's have the well-known Pt characteristic shape, where at low potentials (0.05–0.4 V$_{RHE}$) on the cathodic sweep the hydrogen is adsorbed on the Pt surface while
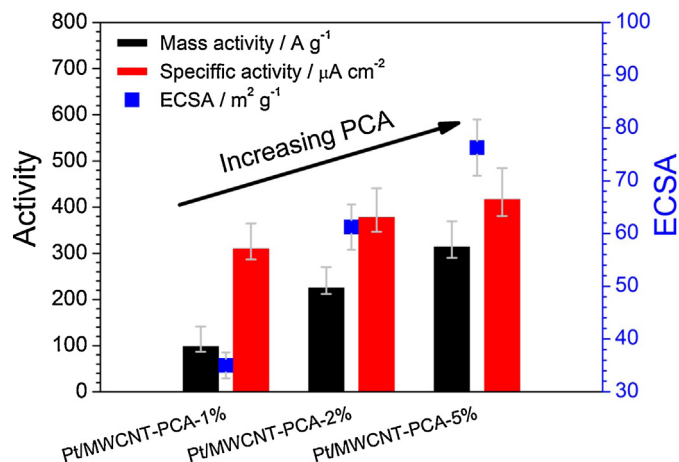


**Fig. 3.** ECSA (square blue scatter), SA (red bar) and MA (black bar) obtained for Pt/MWCNT-PCA-1%, Pt/MWCNT-PCA-2% and Pt/MWCNT-PCA-5%. The activity values are obtained at 0.9 V$_{RHE}$ in 0.1 M HClO$_4$. (For interpretation of the references to colour in this figure legend, the reader is referred to the web version of this article.)

on the anodic sweep hydrogen is desorbed. The Pt-oxide formation specific peaks are formed above 0.8 V$_{RHE}$ on the anodic sweep and it is removed on the cathodic sweep around 0.7 V$_{RHE}$. By 0.4 V$_{RHE}$ the Pt surface is free for the readsorption of hydrogen. Between 0.4 V$_{RHE}$ and approx. 0.7 V$_{RHE}$ the double layer charge is present as a region with no distinct peaks. This region is characteristic for the carbon support and during carbon stressing a wide peak is formed which is known as the hydroquinone–quinone (HQ–Q) redox couple. The ESA was obtained by the integration of the hydrogen desorption region and corrected for the capacitance measured in the double layer region [37]. The ECSA was obtained by dividing the ESA to the Pt electrode mass, thus the largest ECSA was obtained for Pt/MWCNT-PCA-5% with 76.3 m$^2$ g$^{-1}$ followed by Pt/MWCNT-PCA-2% with 61.2 m$^2$ g$^{-1}$ and Pt/MWCNT-PCA-1% with 35 m$^2$ g$^{-1}$ (Fig. 3). Pt/MWCNT-PCA-0% exhibited approx. 20 m$^2$ g$^{-1}$ ECSA. This is close to the Pt black ECSA (13 m$^2$ g$^{-1}$) [31], therefore no further characterization was pursued for this sample. If one assumes that the Pt particles are spherical and that the Pt density is 21.45 g cm$^{-3}$, then for Pt particles with a 3.1 nm diameter, the theoretical ECSA is approx. 90 m$^2$ g$^{-1}$. In this case, the Pt usage is close to 85% for Pt/MWCNT-PCA-5%, 68% for Pt/MWCNT-PCA-2% and 39% for Pt/MWCNT-PCA-1%.

The thin film-rotating disk electrode method was used for estimating the activity towards ORR [38,39]. Hydrodynamic voltammograms were recorded at 400, 900, 1600 and 2500 rpm in an oxygen saturated 0.1 M HClO$_4$ electrolyte and subtracted by the CVs obtained in Ar saturated electrolyte (Fig. S6, Supplementary data, Appendix A). The shape of the ORR voltammograms are resembling those found in literature where the diffusion limiting current at 0.4 V should be approx. −6 mA cm$^{-2}$ [37]. This value is in excellent agreement for all the materials present in Fig. S6 (Supplementary data, Appendix A), with a deviation of less than 5% which means that the larger Pt electrode loading used for Pt/MWCNT-PCA-1% did not significantly affect mass transport. The inset in

**Table 1**
Surface concentration obtained from the deconvolution of the C 1s, Pt 4f and O 1s XPS peaks for Pt/MWCNT-PCA-1%, Pt/MWCNT-PCA-2% and Pt/MWCNT-PCA-5%. OCG means oxygen containing groups.

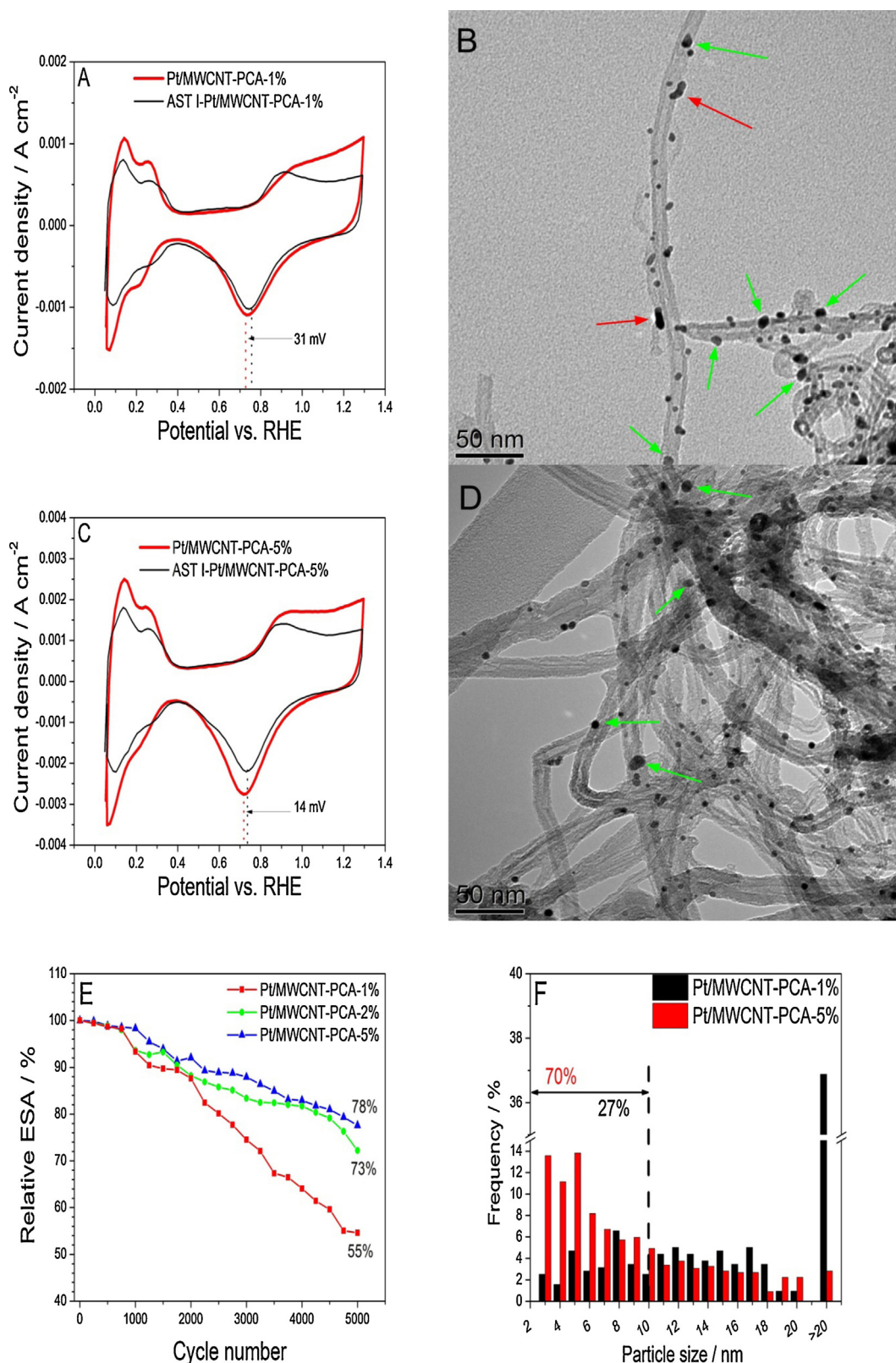| Sample name | C 1s | | | Pt 4f | | | O 1s |
|---|---|---|---|---|---|---|---|
| | sp$^2$ (%) | sp$^3$ (%) | $\pi$–$\pi^*$/(%) | Pt$^0$ (%) | Pt$^{(2+)}$ (%) | Pt$^{(4+)}$ (%) | PtO$_2$ (%) |
| Pt/MWCNT-PCA-1% | 69.2 | 7.6 | 2.1 | 81.7 | 12.1 | 6.2 | 9.5 |
| Pt/MWCNT-PCA-2% | 69.5 | 5.4 | 4.0 | 68.9 | 19.8 | 11.3 | 19.8 |
| Pt/MWCNT-PCA-5% | 70.8 | 3.6 | 5.2 | 64.8 | 23.3 | 11.9 | 26.1 |

**Fig. 4.** CV's for Pt/MWCNT-PCA-1% (A) and Pt/MWCNT-PCA-5% (C) treated with AST I at beginning of testing (BOT, black lines) and at the end of testing (EOT, red lines) with the associated post mortem TEM: Pt/MWCNT-PCA-1% (C) and Pt/MWCNT-PCA-5% (D). The red dotted lines represent the potential at maximum cathodic current between 0.6 and 0.8 $V_{RHE}$ at BOT and black dotted lines at EOT. The green arrows in B and D represent are indicating Pt growth, while the red arrows are indicating Pt coalescence of multiple Pt nanoparticles. The initial Pt electrode loading was kept for all experiments at 20 $\mu g_{Pt}$ cm$^{-2}$. All the experiments took place in an Ar saturated 0.1 M HClO$_4$ electrolyte between 0.05 and 1.3 $V_{RHE}$ at a 0.5 V s$^{-1}$ sweep rate. The relative ESA is plotted against the cycle number in (E). The particle histogram for Pt/MWCNT-PCA-1% (black bar) and Pt/MWCNT-PCA-5% (red bar) are presented in (F)—approx. 250 particles from several TEM images have been counted in order to obtain the histogram. (For interpretation of the references to colour in this figure legend, the reader is referred to the web version of this article.)

Fig. S6 (Supplementary data, Appendix A) is the representative Koutecky–Levich plot at $0.9\,V_{RHE}$ at different rotating speeds normalized to the Pt electrode mass. The slope of the fitted lines results in the number of electrons used for the reaction, which is close to $4\,e^-$ for Pt/MWCNT-PCA-2% and Pt/MWCNT-PCA-5% while for Pt/MWCNT-PCA-1% is closer to $3.5\,e^-$. The intercept on the $y$-axis results shows the MA. This follows the same trend as for the ECSA (Fig. 3).

The effect of adding PCA definitely improves the dispersion of Pt nanoparticles on the support which translates into an increased ECSA and MA, as shown in Fig. 3. The values obtained for Pt/MWCNT-PCA-5% are comparable to the ones reported for Pt supported on active carbon with particle sizes between 2 and 3 nm [31], which means that a good Pt dispersion has been achieved on the MWCNT surface. A 1.5 fold improvement in the MA has been obtained when compared to the covalently functionalized MWC-NTs [40]. In a recent study treated MWCNT with PCA and supported PtRu was used for methanol oxidation. This resulted in a $60\,m^2\,g^{-1}$ ECSA [35], which is still lower than Pt/MWCNT-PCA-5%. In another study a $54.3\,m^2\,g^{-1}$ ECSA and a SA of $4\,A\,m^{-2}$ at 0.78 V [41] was reported, whereas Pt/MWCNT-PCA-5% has an ECSA of $76.3\,m^2\,g^{-1}$ and the SA measured at $0.9\,V_{RHE}$ approx. $4.3\,A\,m^{-2}$. Orfanidi et al. prepared Pt supported on covalently functionalized MWCNT with pyridine and hydroxypyridine with similar catalytic ECSA, SA and MA, nevertheless the work has not pursued any accelerated stress tests [42]. In this respect, we have conducted two different types of accelerated stress tests which are presented in the following sub-section.

### 3.3. Electrochemical stability

In order to study the degradation of the materials discussed in the previous section we have pursued two types of AST; one consisting of potential sweeping between 0.05 and $1.3\,V_{RHE}$ at $0.2\,V\,s^{-1}$ (AST I) and another one consisting of potential sweeping between 1 and $1.5\,V_{RHE}$ at $0.5\,V\,s^{-1}$, as proposed by FCCJ [34] (AST II). Due to the reasons concerning the larger Pt electrode loading for Pt/MWCNT-PCA-1% which was explained in the previous section, the Pt electrode loading has been maintained for all the samples at $20\,\mu g_{Pt}\,cm^{-2}$ during the degradation studies. This has been done for the electrochemical stability in order to prevent any doubt with regards to the fact that more Pt may alter the findings [43]. Fig. 4 shows the changes induced by AST I. With the aim of having a clearer picture on the influence of PCA on the MWCNTs during degradation only Pt/MWCNT-PCA-1% and Pt/MWCNT-PCA-5% are carefully taken in consideration. It is rather easy to distinguish between the transformations occurred under AST I and the ones under AST II. For AST I a combined degradation behaviour is observed consisting of both Pt degradation and carbon support oxidation. This is a rather harsh treatment on the electrocatalyst itself and the support as well due to the excursions at potentials as large as $1.3\,V_{RHE}$ where Pt is completely oxidized [9]. Moreover at $0.4\,V_{RHE}$ the Pt surface is completely reduced, so a continuous Pt oxidation–reduction is taking place which should degrade sufficiently the electrocatalyst. The $H_{UPD}$ region ($0.05–0.4\,V_{RHE}$) is decreasing with the number of cycles which translates into a lower ESA as observed by the trend in Fig. 4. For Pt/MWCNT-PCA-1% there is a very small HQ–Q redox couple between 0.4 and $0.7\,V_{RHE}$ as it can be seen from Fig. 4A, this will give in turn a lower ESA at the end of test (EOT). The reduction peak of the Pt oxide around $0.7\,V_{RHE}$ on the cathodic sweep is shifting towards higher potentials (Fig. 4A and C). The change in this potential is 31 mV for Pt/MWCNT-PCA-1% and 14 mV for Pt/MWCNT-PCA-5%. It is believed that if this peak is situated at larger potentials then the adsorption strength of OH* species is decreasing, therefore decreasing the ORR activity [44,45]. In addition, the shift towards larger potentials can be

attributed to the reduction of Pt oxide at less oxophilic sites, hence larger particles [46]. This is confirmed by Fig. 4, where Pt/MWCNT-PCA-1% retains 55% of the initial ESA while Pt/MWCNT-PCA-2% and Pt/MWCNT-PCA-5%, retains 73% and 78%, respectively. We have recently compared in similar conditions the same MWCNTs with covalently functionalized MWCNTs. The functionalized MWCNTs were found to be more stable at the cost of decreased ORR activity [40]. However, Pt/MWCNT-PCA-5% retains 78% of the initial ESA which is an improvement from the 58% for covalently functionalized MWCNT [40]. Taking into consideration that the support is the same in both studies and the Pt particle size distribution is similar, it can be concluded that there is an interaction between Pt and PCA-MWCNT which may prevent the Pt degradation. This is supported by the XPS findings presented in Section 3.1. Nevertheless, such allegations should be avoided without further supporting evidence. Therefore, post mortem TEM has been performed after the AST I.

Pt degradation has been extensively studied and it was shown that dissolved Pt may redeposit in the ionomer as permeating hydrogen reduces the Pt ions [47,48]. Moreover dissolved Pt has been documented to be present in the fuel cell exit water stream [49]. When looking at the more fundamental Pt degradation this can be 3D Ostwald ripening, 2D Ostwald ripening and coalescence. The difference between the 3D and 2D Ostwald ripening is the path through which dissolved Pt species are travelling. If it is through the electrolyte, then it is called 3D Ostwald ripening while if it is along the carbon surface it is called 2D Ostwald ripening [48,50,51]. The coalescence may be caused by the Pt migration on the support with further "fusion" of Pt nanoparticles in one single larger particle [52]. However, this may be caused from the initial particles which are in contact or from carbon corrosion which shrink forcing Pt nanoparticles to come in contact [53].

Fig. 4B and D shows the post mortem TEM for Pt/MWCNT-PCA-1% and Pt/MWCNT-PCA-5% at EOT after AST I. In the case of Pt/MWCNT-PCA-1% (Fig. 4B) there is an extended Pt degradation. It is well-known now that smaller Pt nanoparticles are more prone to dissolution due to the so called Gibbs-Thomson effect [32]. This can in turn lead to an increased particle size through the 2D/3D Ostwald ripening. This is happening in both samples, Pt/MWCNT-PCA-1% and Pt/MWCNT-PCA-5%, and it cannot be overcome by any current synthesis route. Pt degradation associated with coalescence will increase with increasing Pt loading on the support, due to smaller interparticle distance [51]. So, this can be overcome only if the support has a large enough surface area to house all the Pt nanoparticles on the surface and provide enough interparticle distance in order for the nanoparticles not to be in contact during the fuel cell operation. Further on, the green arrows in Fig. 4 B and D are indicating Pt nanoparticles growth by a degradation mix which may be caused by Pt nanoparticle migration, coalescence and 2D/3D Ostwald ripening. One might consider that there is no difference in the post mortem TEM images for Pt/MWCNT-PCA-1% (Fig. 4B) and Pt/MWCNT-PCA-5% (Fig. 4D), however most of the particles in Fig. 4D are maintaining a spherical shape which is not the case for all the Pt nanoparticles in Fig. 4B. The red arrows in Fig. 4B are highlighting regions where multiple Pt nanoparticles appear to overlap which may indicate coalescence. This may be mainly caused by the presence of the Pt islands on the pristine sample, which are formed of aggregates of Pt nanoparticles (Fig. 1A). The Pt nanoparticles in Pt/MWCNT-PCA-5% are initially in contact for the pristine sample as well (Fig. 1C), however it seems that PCA prevents the formation of such Pt clusters. Fig. 4F shows the particle histograms as obtained from several TEM pictures from which it can be seen that there is an extended Pt degradation with a wide particle size distribution. It is very interesting to observe that for Pt/MWCNT-PCA-5% approx. 70% of the initial particles maintained a size smaller than 10 nm while for Pt/MWCNT-PCA-1% only 27% are found in the same size range. In
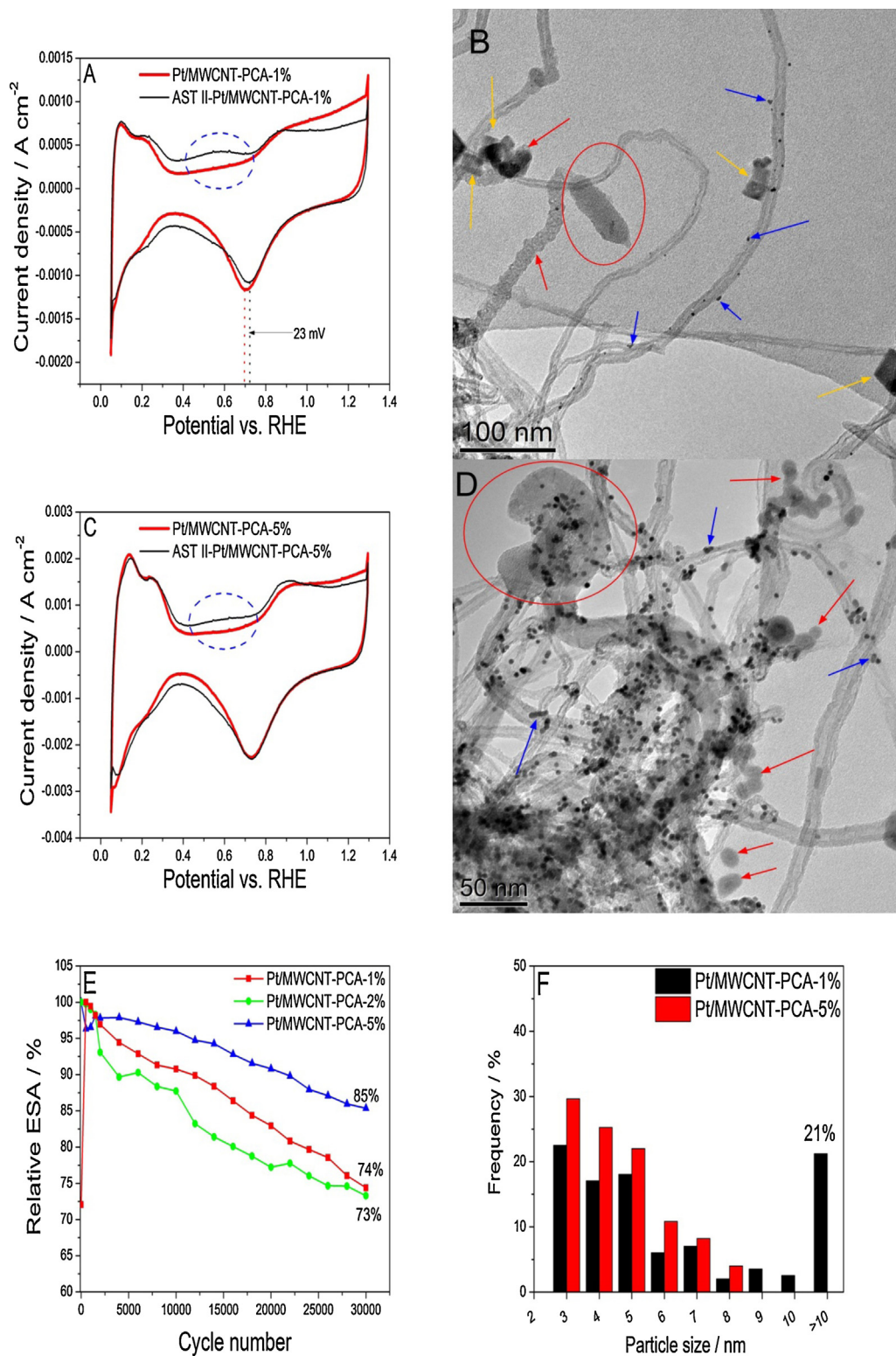
**Fig. 5.** CV's for Pt/MWCNT-PCA-1% (A) and Pt/MWCNT-PCA-5% (C) treated with AST II at BOT (black lines) and EOT (red lines) with the associated post mortem TEM: Pt/MWCNT-PCA-1% (C) and Pt/MWCNT-PCA-5% (D). In the CV's, the red dotted lines represent the potential at maximum cathodic current between 0.6 and 0.8 $V_{RHE}$ at BOT and black dotted lines at EOT; the blue dotted ellipses are showing the appearance of HQ–Q redox couple. In (B) and (D), the blue arrows indicate coalescence of Pt nanoparticles, the orange arrows are indicating possible Pt nanoparticles which have transformed into rectangles, while the red arrows and red ellipses are indicating different steps of MWCNT structural change and corrosion. The initial Pt electrode loading was kept for all experiments at 20 $\mu g_{Pt}$ cm$^{-2}$. All the experiments took place in an Ar saturated 0.1 M HClO$_4$ electrolyte. The relative ESA is plotted against the cycle number in (E). The particle histogram for Pt/MWCNT-PCA-1% (black bar) and Pt/MWCNT-PCA-5% (red bar) are presented in (F)—approx. 250 particles from several TEM images have been counted in order to obtain the histogram. (For interpretation of the references to colour in this figure legend, the reader is referred to the web version of this article.)

the case of Pt/MWCNT-PCA-1%, approx. 40% of the initial particles have diameters larger than 20 nm while for Pt/MWCNT-PCA-5% less than 5% have this size. Taking in consideration that we have tested in similar conditions the same MWCNTs and approx. 50% of the initial ESA was retained [40], therefore the interaction between Pt and PCA-MWCNTs can be held responsible for the improved stability.

Pt degradation was discussed in the first part of the current section. Carbon corrosion and its associated degradation mechanisms are discussed in the following. It is difficult to completely distinguish between Pt degradation and support degradation in spite of their each individual effect. Meier et al. proposed to classify the degradation associated with Pt and carbon corrosion as primary degradation phenomena [52]. Therefore, carbon corrosion as a primary degradation mechanism can lead to particle detachment by corrosion of the Pt-support interface and Pt nanoparticle agglomeration by effective loss of surface area which arises from carbon corrosion. Taking in consideration that both primary degradation phenomena may lead to similar secondary degradation mechanism, it is hard to draw a clear line between each degradation process. However, the FCCJ protocol made a clear cut by subjecting the catalyst to potential excursions as high as 1.5 $V_{RHE}$ with a lower potential limit of 1 $V_{RHE}$ and separating carbon degradation from Pt degradation [34]. One should expect some Pt dissolution below 1.15 $V_{RHE}$ since above 1.15 $V_{RHE}$ a subsurface oxide is formed [9]. Nonetheless, it has been recently confirmed that carbon degradation is the predominant mechanism resulted from the FCCJ protocol [35,54].

The CV's for Pt/MWCNT-PCA-1% (Fig. 5A) and Pt/MWCNT-PCA-5% (Fig. 5C) are showing the samples during AST II at BOT and EOT. In contrast to Fig. 4A and C the $H_{UPD}$ region situated at 0.05–0.4 $V_{RHE}$ is not decreasing in terms of peak current density. However, this is misleading because the double layer charge is increasing leading to a decrease in ESA. The most degraded sample subjected to AST II is, surprisingly, Pt/MWCNT-PCA-2% (73%) which is very close to Pt/MWCNT-PCA-1% (74%) followed by Pt/MWCNT-PCA-5% (85%). It is worth mentioning that the CV at BOT for Pt/MWCNT-PCA-1% is actually after 500 cycles of sweeping between 1 and 1.5 $V_{RHE}$ at 0.5 $V s^{-1}$ due to the small artefact in the initial cycles (Fig. 5E). The appearance of HQ–Q redox couple (0.4–0.8 $V_{RHE}$) is observed as a clear feature for both samples which reflects that the carbon support undergoes some transformation. It is believed that the increase in the double layer charge is caused by different oxygen functional groups on the MWCNT surface. It has been documented that an increased Pt loading results in a more pronounced ESA loss, under similar condition to the one in this study [43]. Similar to Fig. 4A there is a 23 mV difference on the cathodic sweep around 0.7 $V_{RHE}$ for Pt/MWCNT-PCA-1% (Fig. 5A). This is an indication of particle growth as discussed in the first part of this section. Even though for Pt/MWCNT-PCA-1% treated with AST I (Fig. 4A) a larger potential difference is observed (31 mV), there is still a significant change. Interestingly, no difference can be observed around 0.7 $V_{RHE}$ for Pt/MWCNT-PCA-5% treated with AST II (Fig. 5C). Moreover, the reduction of the Pt oxide surface looks strikingly similar for the CV's at EOT and BOT for Pt/MWCNT-PCA-5% with an almost perfect overlay. This is an indication that Pt particles have not increased in diameter to a large extent. In this regard, TEM investigations have been pursued after the degradation test.

Post mortem TEM has been performed since there is a difference between Pt/MWCNT-PCA-1% and Pt/MWCNT-PCA-5% in the reduction potential of Pt surface oxide. Fig. 5B and D shows the post mortem TEM images for Pt/MWCNT-PCA-1% and Pt/MWCNT-PCA-5% subjected to AST II. The blue arrows in Fig. 5B and D indicate Pt nanoparticle coalescence which seems to be more severe for Pt/MWCNT-PCA-1% (Fig. 5B) than for Pt/MWCNT-PCA-5% (Fig. 5D). If one considers that AST II causes predominantly carbon corrosion

then it can be concluded that the reason for Pt nanoparticle coalescence was mainly corrosion of the Pt-support interface or the direct corrosion of MWCNTs which results in a lower surface area, hence Pt nanoparticles coming in contact and forming a larger particle. However, this is happening to a lower extent in case of Pt/MWCNT-PCA-5% where most of the Pt nanoparticles maintain their initial size and shape. Fig. 5F shows the particles histogram from which it is clear that Pt/MWCNT-PCA-5% preserves more particles in their initial size (approx. 3 nm). Pt/MWCNT-PCA-1% has a similar distribution but with a large proportion (i.e. 21%, Fig. 5F) of particles with a diameter larger than 10 nm, which are not found for Pt/MWCNT-PCA-5%.

A large proportion of these particles are rectangular particles as indicated by the orange arrows in Fig. 5B is of a particular interest. This rectangular type of particle is present only in the case of Pt/MWCNT-PCA-1% and Pt/MWCNT-PCA-2%. The size of the rectangular particles is in the range of 10–30 nm. Xie et al. found similar particles at the anode side of the membrane electrode assembly after 1000 h of constant-current testing mode at 1.07 A cm$^{-2}$[55]. Taking into consideration the potential window (1–1.5 $V_{RHE}$) it is hard to believe that such a degradation took place during the actual stress test. It would be more plausible if this transformation actually occurred during the measurement of ESA which took place every 2500 cycles, hence 12 times. This should be accompanied by migration of Pt nanoparticles on the support, which is in line with the findings that PCA enhances the Pt-support interaction.

The red arrows and ellipses in Fig. 5B and D are indicating regions of carbon corrosion. These regions where MWCNTs are undergoing a transformation towards carbon spheres are highly surprising. Another possibility for the appearance of such carbon nanostructures might be the PCA corrosion. Recently, it has been shown that −800 mV needs to be applied in order to remove the PCA from graphite like structures [56]. Even at this negative potential less than 10% is removed from the surface in acidic environment [56]. This means that in the 1–1.5 $V_{RHE}$ potential window PCA is still present. However, the PCA is a structure composed of 4 benzene rings grouped together linked to a carboxylic group which might corrode as well at potentials as high as 1.5 $V_{RHE}$. In this respect, PCA was subjected to AST II in order to remove any suspicion that the PCA might corrode during AST II. CV's at BOT and EOT of PCA coated glassy carbon electrode (GCE) are shown in Fig. S7. The bare GCE has no peak in between 0.4 and 1 $V_{RHE}$. When PCA is added to GCE a wide peak appears, which is centred at 0.67 $V_{RHE}$. At EOT this peak preserves its shape and current magnitude. No decrease in the charge associated with this peak can be observed between the CV at BOT and EOT. This shows clearly that it is highly improbable for the PCA to be the source of the carbon spheres and the MWCNTs are undergoing severe structural and morphological changes.

It seems that during AST II, the rolled graphenes forming the MWCNTs are actually destroyed by the harsh oxidation treatment. To the best of our knowledge, the phenomenon of MWCNT transformation to carbon spheres (CNT-CS) is the first time ever reported. The reader should bear in mind that these MWCNTs are not perfect. That is, there is a large extent of structural defects as it was shown in our previous work [40,57] which can be seen from Figs. 1, 4 and 5 where the MWCNTs are bundled up. The red arrows in Fig. 5B are clearly showing a MWCNT undergoing severe morphological change by swelling from the tip towards the rest of the MWCNT. This is an indication that the CNT-CS process is starting at the tip where unterminated crystallographic planes have a stronger reactivity towards different hydrogen and oxygen functional groups. As discussed in the introduction, the MWCNTs tips have a large density of defects which makes it easier for the MWCNT to be corroded from the tips onwards. The kinks of the basal planes can be the starting points for the carbon corrosion as well due to the free σ-electrons and unsaturated valences [26]. It has been

reported that the oxidation of high surface area carbons acting as a support for Pt are starting at large potentials (above $1\,V_{RHE}$) where defects are created which are subsequently corroded at very low potentials (below $0.7\,V_{RHE}$) [25]. In addition, the reduction of the Pt subsurface oxide layer may provide the additional needed oxygen to end the MWCNTs degradation with $CO_2$ formation. If potential excursions up to $1.5\,V_{RHE}$ in Ar saturated $0.1\,M\,HClO_4$ represents the main cause for this remarkable CNT-CS process, then the acid treatment for MWCNT which takes place in nitric/sulphuric acid mixture should be carefully reconsidered. The lack of further experimental proof calls for additional characterization (such as in situ techniques) in order to clearly establish the CNT-CS process.

## 4. Conclusions

A non-covalent functionalization of MWCNT using 1-pyrenecarboxilic acid (PCA) has been used as an alternative to the usually used acid treatment with the purpose of obtaining a series of support materials for Pt deposition. The good control of the Pt synthesis delivered Pt nanoparticles with a very narrow size distribution which served as standard electrocatalysts in order to study the Pt-support interaction. The mechanism for the interaction between the MWCNTs and PCA has been confirmed by XPS and the existence of an interaction between the Pt nanoparticles and the PCA functionalized MWCNTs acting as a support has been documented. It has been proven that by just changing the MWCNTs surface in a non-damaging manner results in good dispersion of Pt on the MWCNTs surface. Improving the dispersion leads to a greater activity towards the oxygen reduction reaction in acidic medium. Extensive electrochemical stability investigations have been performed from which it was confirmed that the Pt-MWCNT interaction leading to a large improvement in the stability over long term testing. In our attempt to prove that there is an interaction between PCA-MWCNTs and Pt by performing degradation studies, two other interesting findings have been discussed in this work. First, the geometrical transformation of initial spherical Pt nanoparticles into rectangular particles which have 4–5 times the initial dimensions. Second, the transformation of MWCNTs into carbon spheres has been visualized for the first time, to the best of our knowledge. Future work along this line should include the use of in-situ techniques for a better understanding of the phenomena. The findings discussed in this work should provide an insight in the way we think about the "corrosion proof" MWCNTs. Bearing in mind that all the experiments were conducted at room temperature, one should expect an even faster degradation with the increase in temperature. In this respect, one should take into consideration the use of such materials for high temperature PEMFCs (approx. 150 °C).

## Acknowledgements

## Appendix A. Supplementary data

Supplementary data associated with this article can be found, in the online version, at http://dx.doi.org/10.1016/j.apcatb.2014.07.005.

## References

[1] A. Cowley, Platinum 2013—Interim Review, Johnson Matthey, Royston, Hertfordshire, 2013, lang;http://www.platinum.matthey.com/media/1631235/platinum_2013_interim_review.pdf⟩.
[2] M. Lefèvre, E. Proietti, F. Jaouen, J-P. Dodelet, Science 324 (2009) 71–74.
[3] G. Wu, K.L. More, C.M. Johnston, P. Zelenay, Science 332 (2011) 443–447.
[4] D. Papageorgopoulos, DOE Hydrogen and Fuel Cells Program: annual progress report, FY: 2013, http://www.hydrogen.energy.gov/pdfs/progress13/v_0_papageorgopoulos_2013.pdf
[5] J. Greeley, I.E.L. Stephens, S. Bondarenko a, T.P. Johansson, H.a. Hansen, T.F. Jaramillo, et al., Nat. Chem. 1 (2009) 552–556.
[6] I.E.L. Stephens, A.S. Bondarenko, U. Grønbjerg, J. Rossmeisl, I. Chorkendorff, Energy Environ. Sci. 5 (2012) 6744.
[7] R. Srivastava, P. Mani, N. Hahn, P. Strasser, Angew. Chem. Int. Ed. Engl. 46 (2007) 8988–8991.
[8] K. Sasaki, H. Naohara, Y. Cai, Y.M. Choi, P. Liu, M.B. Vukmirovic, et al., Angew. Chem. Int. Ed. Engl. 49 (2010) 8602–8607.
[9] A.A. Topalov, I. Katsounaros, M. Auinger, S. Cherevko, J.C. Meier, et al., Angew. Chem. Int. Ed. Engl. 51 (2012) 12613–12615.
[10] C.A. Reiser, L. Bregoli, T.W. Patterson, J.S. Yi, J.D. Yang, M.L. Perry, et al., Electrochem. Solid-State Lett. 8 (2005) A273.
[11] M. Pourbaix, Atlas of Electrochemical Equilibria in Aqueous Solutions, second ed., Association of Corrosion Engineers, Houston, TX, 1974 (English).
[12] N.R. Elezović, B.M. Babić, V.R. Radmilovic, L.M. Vračar, N.V. Krstajić, Appl. Catal., B: Environ. 140-141 (2013) 206–212.
[13] N.R. Elezovic, B.M. Babic, P. Ercius, V.R. Radmilovic, L.M. Vracar, N.V. Krstajic, Appl. Catal., B: Environ. 125 (2012) 390–397.
[14] S-Y. Huang, P. Ganesan, B.N. Popov, Appl. Catal., B: Environ. 102 (2011) 71–77.
[15] S. Jing, L. Luo, S. Yin, F. Huang, Y. Jia, Y. Wei, et al., Appl. Catal., B: Environ. 147 (2014) 897–903.
[16] P. Justin, P.H.K. Charan, G.R. Rao, Appl. Catal., B: Environ. 144 (2014) 767–774.
[17] S.N. Stamatin, E.M. Skou, ECS Trans. 58 (2013) 1267–1276.
[18] R. Dhiman, S.N. Stamatin, S.M. Andersen, P. Morgen, E.M. Skou, J. Mater. Chem. A 1 (2013) 15509.
[19] N-I. Kim, J.Y. Cheon, J.H. Kim, J. Seong, J-Y. Park, S.H. Joo, et al., Carbon (NY) 72 (2014) 354–364.
[20] M. Wang, F. Xu, Q. Liu, H. Sun, R. Cheng, H. He, et al., Carbon (NY) 49 (2011) 256–265.
[21] P. Luksirikul, K. Tedsree, M.G. Moloney, M.L.H. Green, S.C.E. Tsang, Angew. Chem. Int. Ed. Engl. 51 (2012) 6998–7001.
[22] D. Sebastián, I. Suelves, R. Moliner, M.J. Lázaro, A. Stassi, V. Baglio, et al., Appl. Catal., B: Environ. 132–133 (2013) 22–27.
[23] C. Wang, M. Waje, X. Wang, J.M. Tang, R.C. Haddon, Y. Yan, Nano Lett. 4 (2004) 345–348.
[24] W. Li, C. Liang, W. Zhou, J. Qiu, G. Sun, Q. Xin, J. Phys. Chem. B 107 (2003) 6292–6299.
[25] S. Maass, F. Finsterwalder, G. Frank, R. Hartmann, C. Merten, J. Power Sources 176 (2008) 444–451.
[26] P. Stonehart, Carbon 22 (1984) 423–431.
[27] P. Hernández-Fernández, M. Montiel, P. Ocón, J.L.G. de la Fuente, S. García-Rodríguez, S. Rojas, et al., Appl. Catal., B: Environ. 99 (2010) 343–352.
[28] H. Lv, N. Cheng, S. Mu, M. Pan, Electrochim. Acta 58 (2011) 736–742.
[29] A.O. Al-Youbi, J.L. Gómez de la Fuente, F.J. Pérez-Alonso, A.Y. Obaid, J.L.G. Fierro, M.a. Peña, et al., Appl. Catal., B: Environ. 150-151 (2014) 21–29.
[30] L. Zhao, Z-B. Wang, X-L. Sui, G-P. Yin, J. Power Sources 245 (2014) 637–643.
[31] M. Nesselberger, S. Ashton, J.C. Meier, I. Katsounaros, K.J.J. Mayrhofer, M. Arenz, J. Am. Chem. Soc. 133 (2011) 17428–17433.
[32] Y. Shao-Horn, W.C. Sheng, S. Chen, P.J. Ferreira, E.F. Holby, D. Morgan, Top. Catal. 46 (2007) 285–305.
[33] T.J. Simmons, J. Bult, D.P. Hashim, R.J. Linhardt, P.M. Ajayan, ACS Nano 3 (2009) 865–870.
[34] A. Ohma, K. Shinohara, A. Iiyama, T. Yoshida, A. Daimaru, ECS Trans. 41 (2011) 775–784.
[35] Y. Kuang, Y. Cui, Y. Zhang, Y. Yu, X. Zhang, J. Chen, Chemistry 18 (2012) 1522–1527.
[36] H-S. Oh, H. Kim, Adv. Funct. Mater. 21 (2011) 3954–3960.
[37] K.J.J. Mayrhofer, D. Strmcnik, B.B. Blizanac, V. Stamenkovic, M. Arenz, N.M. Markovic, Electrochim. Acta 53 (2008) 3181–3188.
[38] U.A. Paulus, T.J. Schmidt, H.a. Gasteiger, R.J. Behm, J. Electroanal. Chem. 495 (2001) 134–145.
[39] T.J. Schmidt, H.A. Gasteiger, Rotating thin-film method for supported catalysts, in: W Vielstich, HA Gasteiger, A Lamm (Eds.), Handbook of Fuel Cells: Fundamentals, Technology, Applications, Wiley, Chichester, 2003, p. 316.
[40] S.N. Stamatin, M. Borghei, S. Andersen Ma, S. Veltze, V. Ruiz, E. Kauppinen, E.M. Skou, Int. J. Hydrogen Energy 39 (2014) 8215–8224.
[41] Y. Chen, J. Wang, X. Meng, Y. Zhong, R. Li, X. Sun, et al., J. Power Sources 238 (2013) 144–149.

[42] A. Orfanidi, M.K. Daletou, S.G. Neophytides, Appl. Catal., B: Environ. 106 (2011) 379–389.
[43] J. Speder, A. Zana, I. Spanos, J.J.K. Kirkensgaard, K. Mortensen, M. Arenz, Electrochem. Commun. 34 (2013) 153–156.
[44] H.A. Gasteiger, S.S. Kocha, B. Sompalli, F.T. Wagner, Appl. Catal., B: Environ. 56 (2005) 9–35.
[45] T.J. Schmidt, P.N. Ross, N.M. Markovic, V. Uni, J. Phys. Chem. B (2002) 11970–11979.
[46] K.J.J. Mayrhofer, B.B. Blizanac, M. Arenz, V.R. Stamenkovic, P.N. Ross, N.M. Markovic, J. Phys. Chem. B 109 (2005) 14433–14440.
[47] J. Aragane, H. Urushibata, J. Appl. Electrochem. 26 (1996) 147–152.
[48] P.J. Ferreira, G.J. la O', Y. Shao-Horn, D. Morgan, R. Makharia, S. Kocha, et al., J. Electrochem. Soc. 152 (2005) A2256.
[49] S. Mukerjee, S. Srinivasan, Handbook of Fuel Cells Fundamentals, Technology and Applications, Wiley and Sons, Chichester, UK, 2003.
[50] J. Bett, J. Lundquist, W. E., P. Stonehart, Electrochim. Acta 18 (1973) 343–348.
[51] J.C. Meier, C. Galeano, I. Katsounaros, J. Witte, H.J. Bongard, et al., Beilstein J. Nanotechnol. 5 (2014) 44–67.
[52] J.C. Meier, C. Galeano, I. Katsounaros, A.A. Topalov, A. Kostka, et al., ACS Catal. 2 (2012) 832–843.
[53] K. Schlögl, K.J.J. Mayrhofer, M. Hanzlik, M. Arenz, J. Electroanal. Chem. 662 (2011) 355–360.
[54] A. Zana, J. Speder, M. Roefzaad, L. Altmann, M. Baumer, M. Arenz, J. Electrochem. Soc. 160 (2013) F608–F615.
[55] J. Xie, D.L. Wood, K.L. More, P. Atanassov, R.L. Borup, J. Electrochem. Soc. 152 (2005) A1011.
[56] M. Cao, A. Fu, Z. Wang, J. Liu, N. Kong, X. Zong, H. Liu, J. Justin Gooding, J. Phys. Chem. C 118 (2014) 2650–2659.
[57] S. Andersen Ma, M. Borghei, R. Dhiman, H. Jiang, V. Ruiz, E. Kauppinen, E.M. Skou, Carbon 71 (2014) 218–228.